Supplementary Information

Understanding the reversible charging/discharging mechanism of Li_3BO_3 for thermochemical energy storage: an experimental and computational study

Yang Yang [a, #], Yuanqiang Duan [a, #], Wenhao Jiang [b], Xiangqian Du [b], Yushuang Jiang [a], Hongjian Tang [a, *], Lunbo Duan [a, *]

[a] Key Laboratory of Energy Thermal Conversion and Control of Ministry of Education, School of Energy and Environment, Southeast University, Nanjing 211189, China

[b] MCC Huatian Engineering and Technology Corporation, Nanjing, 210019, China

* Corresponding author email address

tanghongjian@seu.edu.cn, duanlunbo@seu.edu.cn

[#] These authors contributed equally to this study.

Contents

S1. Computational Details

S1.1 Parameter settings of First-principles calculation

All first-principles calculations in this study were based on density functional theory (DFT) and performed using the Vienna Ab initio Simulation Package (VASP 5.4.4).[1] The exchange-correlation energy was treated via the Perdew–Burke–Ernzerhof (PBE)[2] functional within the generalized gradient approximation (GGA)[3] and the interaction between ionic cores and valence electrons was described by using the projector augmented wave (PAW) method.[4] The pseudopotentials were taken from the VASP 2020 standard library, and the electron configurations of the atoms were set as follows: Li: $1s^2\ 2s^2$, O: $2s^2\ 2p^4$, B: $2s^2\ 2p^1$, C: $2s^2\ 2p^2$. A plane-wave cutoff energy of 520 eV was used for all systems, with an electronic self-consistency energy convergence threshold of 1×10^{-5} eV. The ionic relaxation termination criterion was set to a Hellmann–Feynman force on each atom smaller than 0.02 $eV\cdot Å^{-1}$.[5] Pulay stress corrections[6] were applied to the total energies of all systems to eliminate basis set errors arising from differences in unit cell shape and volume, ensuring the comparability of energies between different phases.

For the solid-phase calculations, crystals such as Li_3BO_3, $Li_4B_2O_5$, $Li_6B_4O_9$, Li_2CO_3, $Li_2B_4O_7$, and $LiBO_2$ were considered. The initial structures were obtained from the experimental crystallography database (PDF-5+)[7] and the lattice parameters are shown in **Table S1**. Lattice constants and atomic coordinates were fully optimized without symmetry constraints (i.e., optimizing the cell shape, volume, and atomic positions simultaneously) to obtain the corresponding theoretical ground-state structures. The k-point mesh for the Brillouin zone was generated via the Monkhorst-Pack scheme, and its density was validated through energy convergence tests. The specific k-point meshes used for each phase were as follows, $LiBO_2$: 8×8×6, $Li_2B_4O_7$: 5×5×5, Li_2CO_3: 4×7×6, Li_3BO_3: 10×4×4, $Li_4B_2O_5$: 3×7×4, $Li_6B_4O_9$: 10×1×4.

To simulate isolated gas-phase CO_2 molecule, they were placed at the center of a 20 Å × 20 Å × 20 Å cubic supercell to eliminate periodic interactions, with only the Gamma point used for k-mesh sampling. The molecular structure was optimized until the atomic forces were smaller than

0.001 $eV \cdot Å^{-1}$, yielding a bond length of 1.16 Å and a bond angle of 180°. Based on this geometrically relaxed structure, force constants were calculated using Density Functional Perturbation Theory (DFPT),[8] and the vibrational eigenmodes (symmetric stretching, doubly degenerate bending, and antisymmetric stretching) and their frequencies were obtained through diagonalization of the force constant matrix.

These unified parameters and procedures ensure internal consistency in energy, force, and frequency calculations for both solid and gas phases, providing a reliable foundation for subsequent thermodynamic and phase diagram analysis.

Table S1. Lattice parameters of the studied crystals used in the calculations.

Materials	**Space group**	**Structure parameters**
Li_3BO_3	P21/c (No.14)	a = 3.265 b = 9.18 c = 8.316 β = 101.05°
$Li_4B_2O_5$	I2/a (No.15)	a = 10.2269 b = 4.6988 c = 8.7862 β = 93.562°
$Li_6B_4O_9$	P21/n (No.14)	a = 3.31913 b = 23.361 c = 9.1582 β = 92.65°
Li_2CO_3	C2/c (No.15)	a = 8.725 b = 4.9 c = 6.4 β = 116.231°
$Li_2B_4O_7$	P 1 (No.1)	a = 8.48279 b = 8.48278 c = 8.4827 α = 112.3038° β = 112.3038° γ = 103.9428°
$LiBO_2$	P 1 (No.1)	a = 4.35918 b = 5.77107 c = 6.37397 α = 113.5640° β = 90° γ = 90°

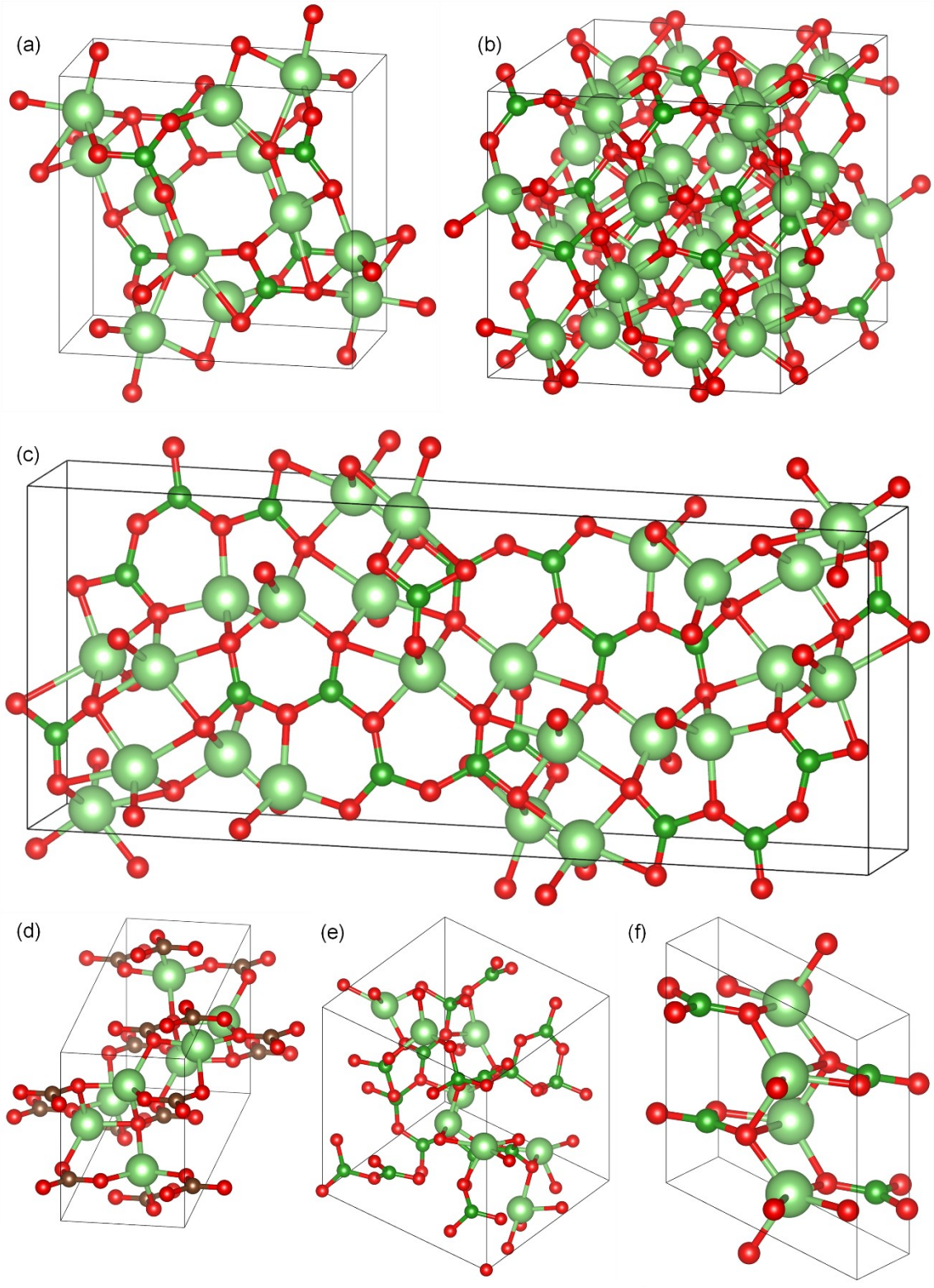

Figure S1. Crystal structure of (a) Li_3BO_3; (b) $Li_4B_2O_5$; (c) $Li_6B_4O_9$; (d) Li_2CO_3; (e) $Li_2B_4O_7$; (f) $LiBO_2$.

S1.2 Phonon and Thermodynamic Property Calculations

Phonon and thermodynamic properties were calculated based on the optimized ground-state crystal structures. Second-order force constants were computed using Density Functional Perturbation Theory (DFPT).[8] To ensure the accuracy of the force constant matrix, stricter convergence criteria were applied in the DFPT calculations: the energy convergence threshold for the electronic self-consistent loop was set to 1×10^{-8} eV, and the Hellmann-Feynman forces on all atoms were required to be less than 1×10^{-7} eV·Å^{-1}. The q-point sampling mesh used for force constant calculations had the same density as the k-point mesh employed for the electronic structure calculations, ensuring consistency between energy and vibrational properties.

Subsequently, the dynamical matrix was Fourier interpolated using Phonopy 2.0.0[9, 10] to obtain the phonon dispersion relations and the phonon density of states, $g(\omega)$, with the normalization condition $\int g(\omega)\mathrm{d}\omega = 3N$ (where N is the number of atoms in the unit cell). Under the harmonic approximation, the phonon density of states $g(\omega)$ was used to calculate the vibrational thermodynamic quantities of the solid, including the Helmholtz free energy (F_{ph}), vibrational internal energy (U_{ph}), and vibrational entropy (S_{ph}). These thermodynamic quantities are temperature-dependent and were calculated over the temperature range of 0–2000 K, with a step size of 10 K to ensure smooth temperature-dependent curves. The frequency integrals were computed using the adaptive Gauss-Legendre method,[11] and the convergence was verified. The expressions for the Helmholtz free energy (F_{ph}), vibrational internal energy (U_{ph}), and vibrational entropy (S_{ph}) are as follows:

$$F_{\mathrm{ph}} = \int_0^{\infty} g(\omega)\left[\frac{1}{2}\mathrm{h}\omega + k_{\mathrm{B}}T\ln(1-e^{-\mathrm{h}\omega/(k_{\mathrm{B}}T)})\right]\mathrm{d}\omega \quad \backslash\text{*MERGEFORMAT(S1)}$$

$$U_{\mathrm{ph}}(T) = \int_0^{\infty} g(\omega)\left[\frac{1}{2}\mathrm{h}\omega + \frac{\mathrm{h}\omega}{e^{\mathrm{h}\omega/(k_{\mathrm{B}}T)}-1}\right]\mathrm{d}\omega \quad \backslash\text{* MERGEFORMAT (S2)}$$

$$S_{\mathrm{ph}}(T) = \frac{U_{\mathrm{ph}}(T) - F_{\mathrm{ph}}(T)}{T} \quad \backslash\text{* MERGEFORMAT (S3)}$$

where $g(\omega)$ is the phonon density of states, ω is the angular frequency, $\hbar$ is the reduced Planck constant, k_B is the Boltzmann constant, and T is the thermodynamic temperature.

At atmospheric pressure, the Gibbs free energy of the solid (G_{solid}) is approximately given by:

$$G_{solid}(T, P_0) \approx E_{DFT} + F_{ph}(T) \quad \text{* MERGEFORMAT (S4)}$$

where E_{DFT} is the electronic ground-state energy at 0 K, and P_0 is the pressure at standard conditions (1bar).

The molar Gibbs free energy of gas-phase CO_2 (G_{CO_2}) is given by the sum of the electronic energy and the translational, rotational, and vibrational degrees of freedom. The overall expression and its components are as follows:

$$G_{CO_2}(T, P) = E_{DFT} + G_{trans}(T, P) + G_{rot}(T) + G_{vib}(T) \quad \text{* MERGEFORMAT (S5)}$$

$$G_{trans} = -k_B T \ln\left[\frac{(2\pi M_{CO_2} k_B T)^{3/2}}{h^3} \cdot \frac{k_B T}{P}\right] \quad \text{* MERGEFORMAT (S6)}$$

$$G_{rot} = -k_B T \ln\left(\frac{T}{\sigma \theta_{rot}}\right), \ \theta_{rot} = \frac{\hbar^2}{2 I k_B}, \ \sigma = 2 \quad \text{* MERGEFORMAT (S7)}$$

$$G_{vib} = \sum_i \left[\frac{1}{2}\hbar\omega_i + k_B T \ln(1 - e^{-\hbar\omega_i/(k_B T)})\right] \quad \text{* MERGEFORMAT (S8)}$$

where G_{trans} is the translational contribution, G_{rot} is the rotational contribution, G_{vib} is the vibrational contribution, P is the partial pressure of CO_2 gas, M_{CO2} is the molecular mass of CO_2, h is Planck's constant, I is the moment of inertia, and σ is the symmetry number. The correction at any pressure is given by:

$$G_{CO_2}(T, P) = G_{CO_2}(T, P_0) + RT \ln\left(\frac{P}{P_0}\right) \quad \text{* MERGEFORMAT (S9)}$$

where R is the gas constant.

S1.3 Phase Diagram and Reaction Construction

The phase diagram reference data is derived from PBE/PAW calculations at 0 K from the Materials Project (MP) database. The formation enthalpy of the compound $Li_aB_bO_c$ is defined as:

$$\Delta H_f^0(\mathrm{Li}_a\mathrm{B}_b\mathrm{O}_c) = E_{\mathrm{DFT}}(\mathrm{Li}_a\mathrm{B}_b\mathrm{O}_c) - a\mu_{\mathrm{Li}}^0 - b\mu_{\mathrm{B}}^0 - c\mu_{\mathrm{O}}^0 \backslash * \text{ MERGEFORMAT} \quad \text{(S10)}$$

where $\Delta H0\ f$ is the formation enthalpy at 0 K, and μ_{Li}, μ_B, and μ_O are the chemical potentials referenced to bulk bcc Li, α-rhombohedral boron, and half of the total energy of an O_2 molecule, respectively. The values of *a*, *b*, and *c* are the stoichiometric coefficients. A negative formation enthalpy indicates that the compound is more stable relative to its constituent elements. Points lying on the convex hull correspond to thermodynamically stable phases, and the line connecting two stable phases represents the equilibrium relationship between the two phases. The carbonation reactions studied in this work are constructed from linear combinations of convex hull stable phases.

S1.4 Carbonation Reaction Equilibrium

To quantitatively determine the temperature-pressure equilibrium relationship of the carbonation reaction, the reaction chemical potential difference is defined as follows:

$$\Delta\mu(T,P) = \sum_i \nu_i G_i(T,P) \quad \text{* MERGEFORMAT (S11)}$$

where $\Delta\mu$ is the reaction chemical potential difference, ν_i is the stoichiometric coefficient (positive for products and negative for reactants), and G_i is the Gibbs free energy of component i. Substituting and rearranging the expressions for the solid and gas phase free energies yields:

$$\Delta\mu(T,P) = \Delta E_{\mathrm{DFT}} + \Delta F_{\mathrm{ph}}(T,P_0) - G_{\mathrm{CO_2}}(T,P_0) + RT\ln\left(\frac{P}{P_0}\right) \quad \text{* MERGEFORMAT (S12)}$$

where ΔE_{DFT} is the difference in electronic energy at 0 K between the solid products and reactants, $\Delta F_{\mathrm{ph}}(T,P_0)$ is the difference in solid-phase vibrational free energy at standard pressure, and $G_{\mathrm{CO_2}}(T,P_0)$ is the molar Gibbs free energy of gas-phase CO_2 at standard pressure. From the equilibrium condition $\Delta\mu(T,P_{\mathrm{eq}}) = 0$, we obtain:

$$P_{\mathrm{eq}}(T) = P_0 \exp\left[-\frac{\Delta\mu^0(T)}{RT}\right] \quad \text{* MERGEFORMAT (S13)}$$

where P_{eq} is the equilibrium CO_2 partial pressure, and $\Delta\mu^0$ is the chemical potential difference at standard pressure P_0, expressed as follows:

$$\Delta\mu^0(T) = \Delta E_{\mathrm{DFT}} + \Delta F_{\mathrm{ph}}(T,P_0) - G_{\mathrm{CO_2}}(T,P_0) \quad \text{* MERGEFORMAT (S14)}$$

Thus, the pCO$_2$-T phase diagram for the carbonation reaction can be derived, where $\Delta\mu < 0$ corresponds to the carbonation region, and $\Delta\mu > 0$ corresponds to the regeneration region.

S1.5 Ion Migration Energy Barrier

The Minimum Energy Path (MEP) and energy barrier for ion migration were obtained using the Climbing Image Nudged Elastic Band (CI-NEB) method.[12] We constructed the initial state (IS) and final state (FS) within the optimized lattice supercell, with the only difference between them being the position of the migrating ion. Three intermediate images were linearly inserted between the IS and FS, resulting in a total of five images forming the elastic band. A spring constant of 5 $eV \cdot Å^{-2}$ was applied along the path direction to maintain an even distribution of images, and the highest-energy image was designated as the climbing image to converge to the saddle point. Optimization was performed using the modified conjugate gradient algorithm, with the convergence criterion being the maximum atomic force perpendicular to the path direction on each image being less than 0.02 $eV \cdot Å^{-1}$. The plane-wave cutoff energy and k-point mesh were consistent with the main calculations, and the minimum lengths of the supercell along the a, b, and c directions were all greater than 9 Å to suppress image interactions. The migration energy barrier is defined as:

$$\Delta E_{\text{barrier}} = E_{\text{TS}} - E_{\text{IS}} \qquad \backslash* \text{ MERGEFORMAT (S15)}$$

where $\Delta E_{\text{barrier}}$ is the migration energy barrier, E_{TS} is the total energy of the transition state image, and E_{IS} is the total energy of the initial state image. By systematically comparing the migration paths and energy barriers for Li^{+} and O^{2-}, the diffusion-interface limitations and rate-controlling steps in the carbonation-regeneration cycle can be clearly identified.

S1.6 Isothermal Kinetics

Isothermal carbonation kinetics were analyzed using the Avrami-Erofeev model[13], whose basic form is:

$$\alpha(t) = 1 - \exp\left[-(kt)^n\right] \qquad \text{* MERGEFORMAT (S16)}$$

where $\alpha(t)$ is the reaction conversion rate, defined as

$$\alpha(t) = \frac{q_t}{q_\infty} \qquad \text{* MERGEFORMAT (S17)}$$

where q_t and q_∞ are the adsorbed amount at time t and the theoretical maximum adsorption capacity, respectively, k is the isothermal effective rate constant (s^{-1}), n is the Avrami index, and t is the reaction time. Taking the natural logarithm of both sides of the equation twice results in the linearized form:

$$\ln(-\ln(1-\alpha(t)) = n \cdot \ln(t) + n \cdot \ln(k) \qquad \text{* MERGEFORMAT (S18)}$$

Using $\ln(t)$ as the x-axis and $\ln(-\ln(1-\alpha(t))$ as the y-axis, the slope and intercept correspond to n and $n \cdot \ln(k)$, respectively. The formal fitting was performed using the Levenberg–Marquardt nonlinear least squares algorithm[11], directly applied to equation (S16). To minimize systematic deviations caused by the induction period and late-stage diffusion limitations, the fitting data window was chosen with $\alpha \in [0.1, 0.9]$. The parameter uncertainties were assessed using the covariance matrix. Here, $n > 1$ indicates accelerated kinetics, typically associated with the coexistence of continuous nucleation and multidimensional interface growth. Conversely, $n < 1$ indicates decelerated kinetics, often related to rapid site saturation or product layer densification leading to diffusion control. k is the isothermal effective rate constant, and a higher value at a given temperature indicates a faster overall reaction progress.

S2. Additional Supporting Figures and Tables

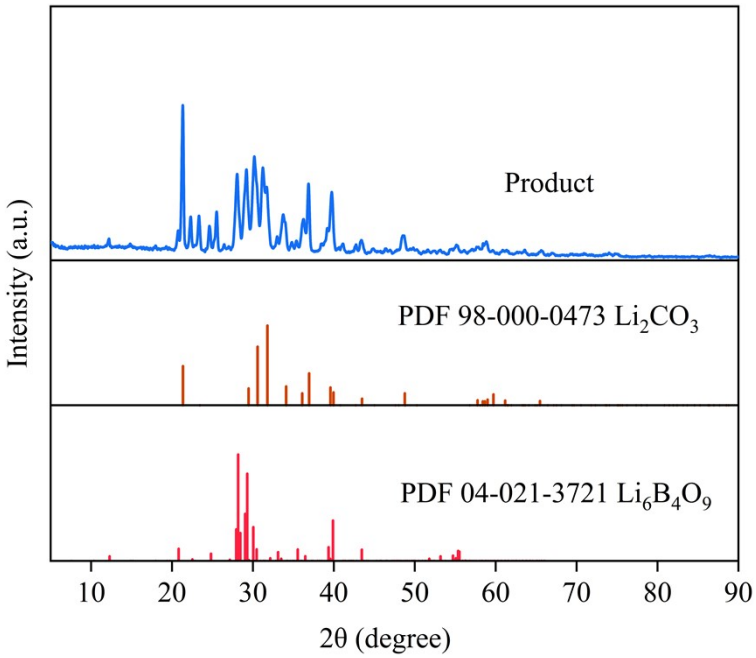

Figure S2. XRD patterns of the discharge products of Li_3BO_3. The reference peak positions (stick patterns) are from the ICDD Powder Diffraction File (PDF) cards for Li_2CO_3 (PDF 98-000-0473) and $Li_6B_4O_9$ (PDF 04-021-3721), used for phase identification.

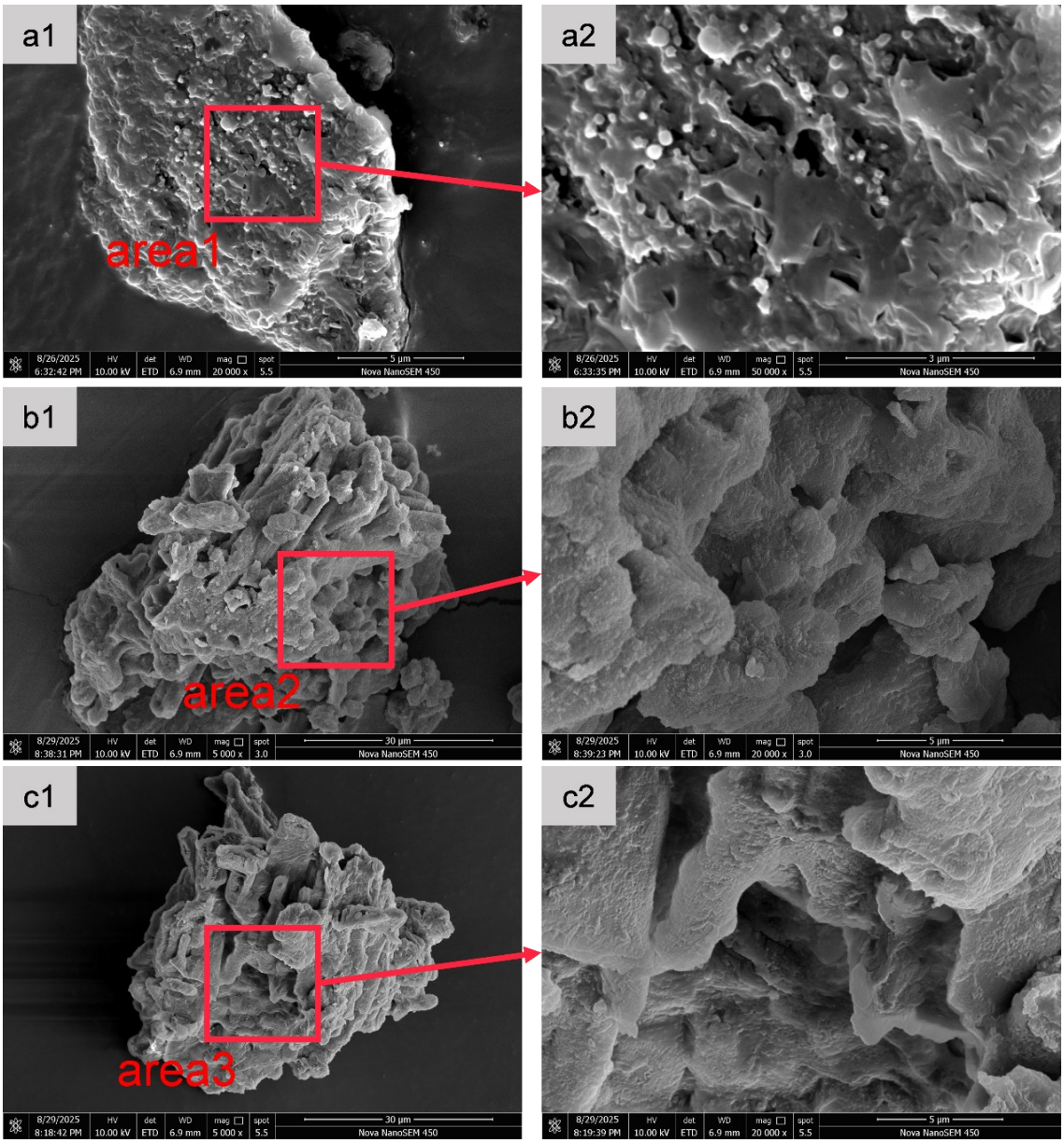

Figure S3. SEM images of Li_3BO_3: (a1, a2) fresh sample, (b1, b2) after the 1st discharge–charge cycle, and (c1, c2) after 10 cycles. The red boxes mark the regions selected for magnification; the corresponding higher-magnification views are shown in (a2), (b2), and (c2), respectively.

Table S2 Rietveld-refined phase fractions of Li_3BO_3 carbonation products at selected temperatures. Note: the weight fractions (wt %) of Li_3BO_3, $Li_4B_2O_5$, Li_2CO_3 and $Li_6B_4O_9$ were quantified from in-situ XRD patterns by Rietveld refinement using JADE (values in parentheses refer to the estimated standard deviations). R (%) and R/E are the profile residual and the goodness-of-fit metric reported by JADE for each refinement.

Temperature (°C)	Li_3BO_3 (wt %)	$Li_4B_2O_5$ (wt %)	Li_2CO_3 (wt %)	$Li_6B_4O_9$ (wt %)	R (%)	R/E
50	100.0 (3.1)	0.0 (0.0)	0.0 (0.0)	0.0 (0.0)	21.3	1.24
400	61.2 (2.1)	0.0 (0.0)	28.5 (0.9)	10.3 (1.2)	23.9	1.39
450	60.0 (2.2)	0.0 (0.0)	28.3 (1.2)	11.8 (1.2)	22.1	1.27
500	39.8 (1.6)	3.5 (1.0)	35.0 (1.2)	21.8 (1.5)	24.9	1.43
550	5.1 (1.3)	10.0 (1.8)	54.6 (1.3)	30.2 (1.2)	26.0	1.49
580	8.8 (1.5)	0.0 (0.0)	66 (2.4)	25.2 (2.3)	28.6	1.64

Table S3 Heat storage capacity and CO_2 capacities of different materials at the first and final cycles.

Compound	Discharging/Charging conditions	Cycle number	TCES capacity ($J \cdot g_{sorbent}^{-1}$)		CO_2 uptake ($g_{CO_2} \cdot g_{sorbent}^{-1}$)		Ref.
			initial	last	initial	last	
CaO	100% CO_2; 600 °C/ 100% N_2; 900 °C	20	3000	430	0.41	0.11	14
SrO	CO_2 1 bar; 875 °C/ CO_2 0.01 bar; 900 °C	10	2260	250	0.43	0.05	15
Li_4SiO_4	100% CO_2; 650 °C/ 100% N_2; 700 °C	10	600	500	0.39	0.31	16
Li_3BO_3	100% CO_2; 560 °C/ 100% N_2; 560 °C	30	1110	1146	0.31	0.32	This work

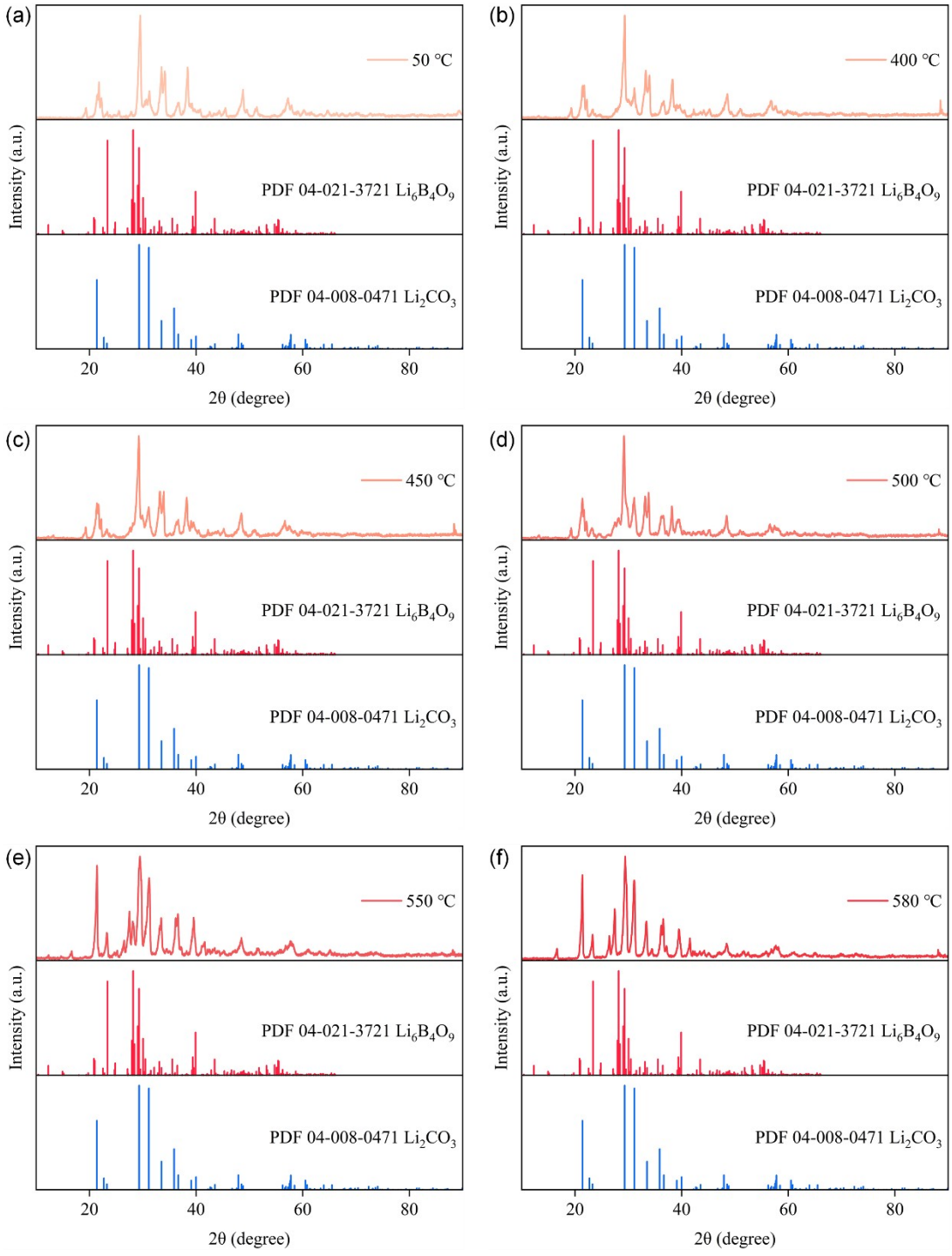

Figure S4. In situ XRD patterns of Li_3BO_3 collected under 100% CO_2 at elevated temperatures: (a) 50 °C, (b) 400 °C, (c) 450 °C, (d) 500 °C, (e) 550 °C, and (f) 580 °C. The stick patterns correspond to the ICDD PDF reference cards of Li_2CO_3 (PDF 04-008-0471) and $Li_6B_4O_9$ (PDF 04-021-3721) for phase identification.

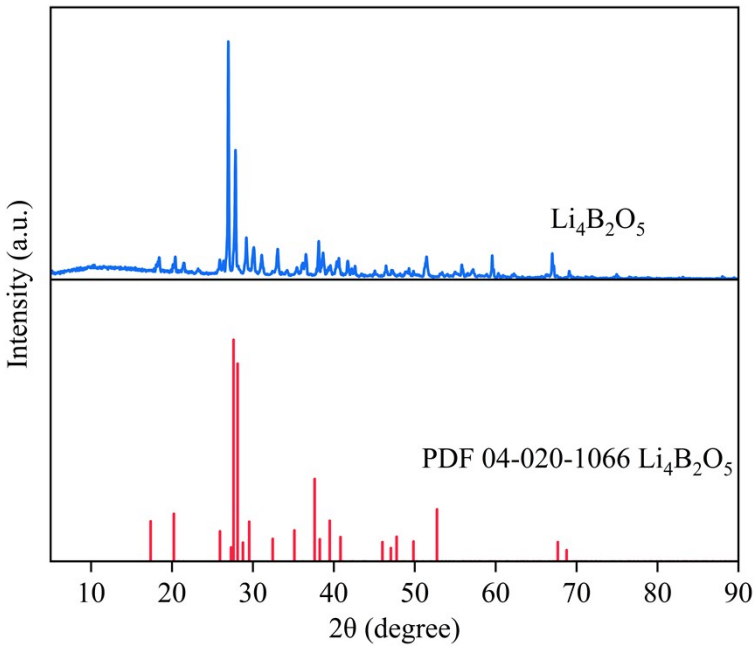

Figure S5. XRD pattern of $Li_4B_2O_5$. The reference peak positions (stick pattern) are taken from the ICDD Powder Diffraction File (PDF) card for $Li_4B_2O_5$ (PDF 04-020-1066) for phase identification.

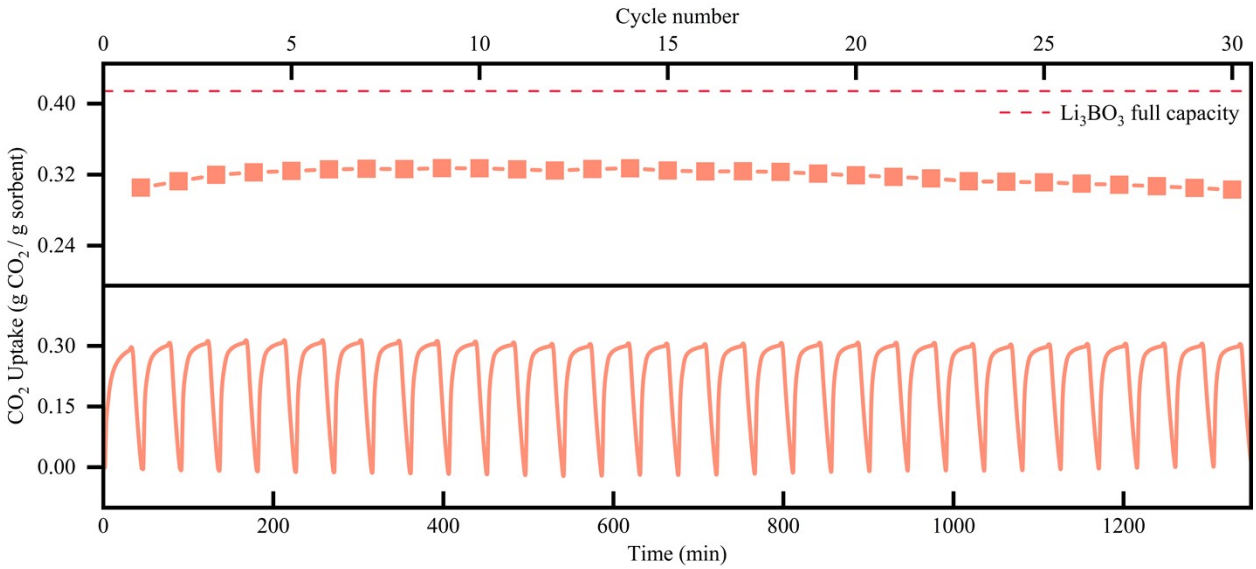

Figure S6. CO_2 uptake capacities of Li_3BO_3 for each cycle and TGA curves of Li_3BO_3 over 30 carbonation/regeneration cycles at 550 °C (carbonation under 100% CO_2 and regeneration under 100% N_2).

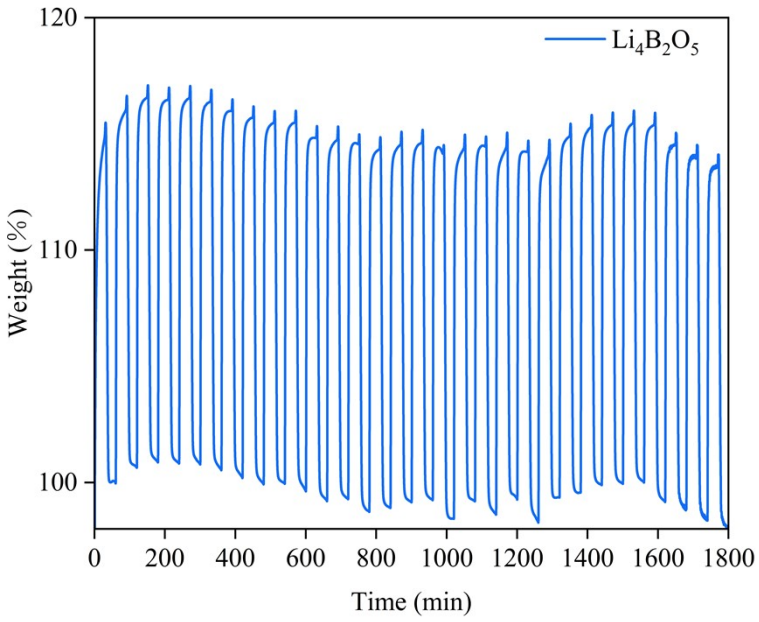

Figure S7. TGA curves of $Li_4B_2O_5$ over 30 charging–discharging cycles at 560 °C (discharging under 100% CO_2 and charging under 100% N_2 atmosphere).

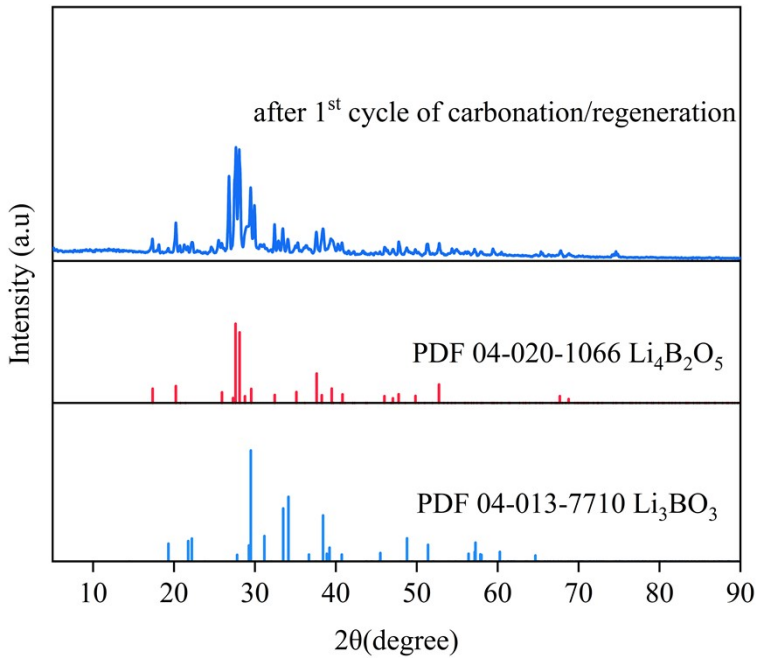

Figure S8. XRD pattern of the charged product after discharge of $Li_4B_2O_5$. The diffraction pattern is compared with the ICDD PDF reference cards for $Li_4B_2O_5$ (PDF 04-020-1066) and Li_3BO_3 (PDF 04-013-7710); stick patterns indicate the standard Bragg reflection positions used for phase assignment.

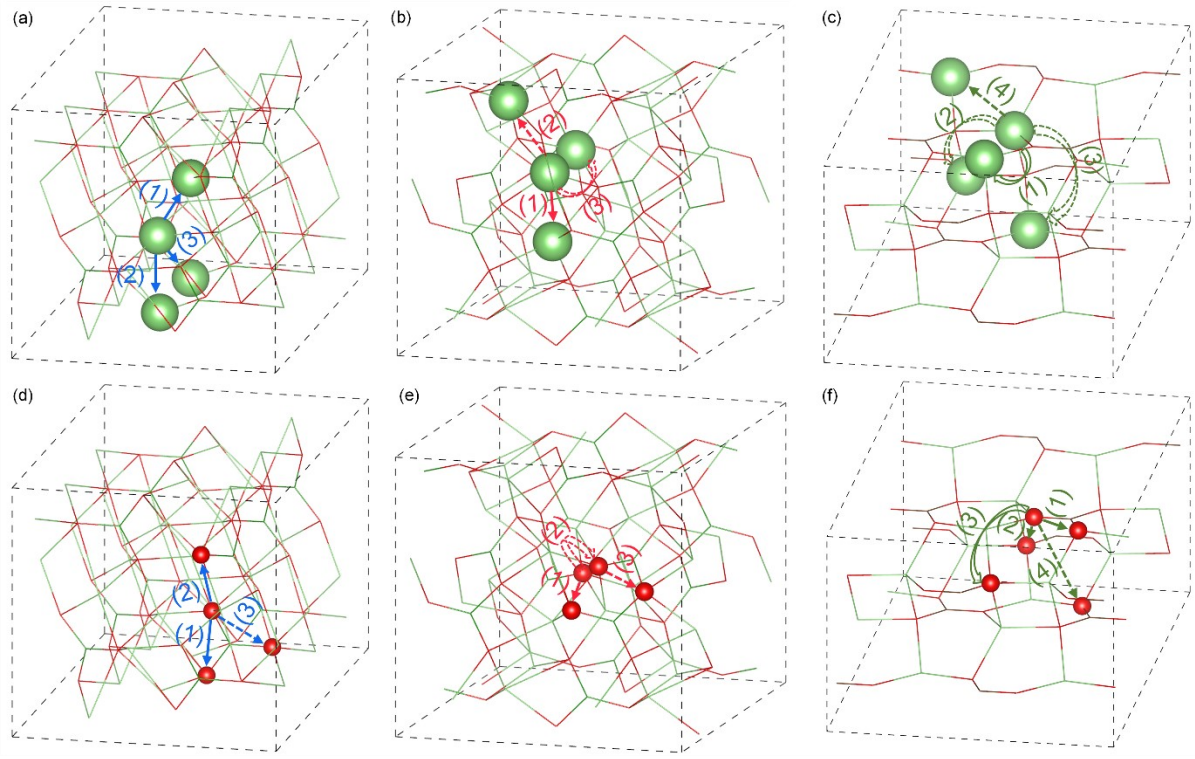

Figure S9. (a) Li^+ hop candidates in Li_3BO_3; (b) Li^+ hop candidates in $Li_4B_2O_5$; (c) Li^+ hop candidates in Li_2CO_3; (d) O^{2-} hop candidates in Li_3BO_3; (e) O^{2-} hop candidates in $Li_4B_2O_5$; (f) O^{2-} hop candidates in Li_2CO_3. For these lattices, migration models were generated for crystallographically inequivalent Li^+/ O^{2-} sites. Candidate single-ion hops were initialized between neighboring sites according to nearest-neighbor connectivity/shortest hop distances and refined by CI-NEB to locate the minimum-energy path (MEP) and a first-order saddle point (TS). Solid arrows denote pathways that converge robustly to reproducible transition states, whereas dashed arrows denote candidates that do not converge to a well-defined first-order saddle point under the present setup.

Table S4. The *n* values obtained at 560 °C by fitting of the experimental curves (**Fig. 6b**) using Avrami–Erofeev model for carbonation reaction.

Material	Stage I	Stage II	Stage III
	n_1	n_2	n_3
Li_3BO_3	1.646	0.466	0.162
$Li_4B_2O_5$	1.176	0.547	N.A.

N.A. indicate the *n* value for $Li_4B_2O_5$ is not available when fitting the Avrami–Erofeev model. Namely, only two Stage II was revealed for $Li_4B_2O_5$ carbonation.

Table S5. Experimental and fitted α values for the carbonation of Li_3BO_3 and $Li_4B_2O_5$.

Li_3BO_3			$Li_4B_2O_5$		
Time (s)	α_{exp}	α_{fit}	Time (s)	α_{exp}	α_{fit}
34.0002	0.071653	0.084213	34.0002	0.068607	0.071194
39	0.099493	0.104409	37.9998	0.082069	0.080732
43.9998	0.125549	0.125851	43.0002	0.096884	0.092765
51	0.160121	0.157623	48	0.110112	0.104885
58.0002	0.194958	0.191031	54	0.123457	0.119504
66	0.23421	0.230691	61.0002	0.13933	0.136613
75	0.275489	0.276545	69	0.155556	0.156172
85.9998	0.310615	0.326692	76.9998	0.172428	0.175679
97.9998	0.333776	0.343217	87	0.19371	0.199915
112.0002	0.354138	0.360725	97.9998	0.22381	0.226298
127.0002	0.372907	0.377764	109.9998	0.253204	0.254657
145.0002	0.393197	0.396309	124.0002	0.286949	0.287086
166.0002	0.412738	0.415828	139.0002	0.323868	0.32094
189	0.432859	0.435096	157.0002	0.362316	0.360236
216	0.454041	0.455453	175.9998	0.396825	0.400044
247.0002	0.476864	0.476405	198	0.425103	0.441613
280.9998	0.500169	0.496995	223.0002	0.451734	0.463083
321	0.523257	0.518651	250.9998	0.475661	0.48497
367.0002	0.546683	0.540811	282	0.498648	0.506991
418.0002	0.569095	0.562638	316.9998	0.521869	0.529531
477	0.590663	0.585021	357	0.546972	0.552791
544.9998	0.612111	0.607781	400.9998	0.572898	0.575828
622.0002	0.631025	0.630441	451.0002	0.598589	0.599332
709.9998	0.64965	0.653135	507	0.624339	0.622871
810	0.666707	0.675653	571.0002	0.648618	0.646817

924	0.682823	0.700724	642	0.673016	0.670363
1055	0.697201	0.708472	721.9998	0.696767	0.693789
1204	0.710495	0.716153	811.9998	0.721164	0.716948
1374	0.722774	0.72379	913.0002	0.744503	0.739673
1568	0.733872	0.73138	1027	0.767078	0.761979
1789	0.744101	0.738907	1155	0.789712	0.78363
2042	0.752714	0.746402	1299	0.809935	0.80456
2330	0.760531	0.753819	1461	0.829806	0.824661
2659	0.767551	0.76118	1643	0.847266	0.843806
3035	0.77392	0.768484	1848	0.862904	0.861951
3464	0.779324	0.775712	2079	0.878483	0.879014
3953	0.783957	0.782856	2338	0.89177	0.894848
4511	0.788203	0.789918	2629	0.904997	0.909445
5148	0.792087	0.796899	2957	0.917519	0.922814
5875	0.79573	0.803793	3326	0.928571	0.934907

References

1. G. Kresse and J. Furthmüller, *Computational Materials Science*, 1996, **6**, 15–50.
2. J. P. Perdew, K. Burke and M. Ernzerhof, *Physical Review Letters*, 1996, **77**, 3865–3868.
3. A. D. Becke, *The Journal of Chemical Physics*, 1993, **98**, 5648–5652.
4. P. E. Blöchl, *Physical Review B*, 1994, **50**, 17953–17979.
5. G. Kresse and J. Furthmüller, *Phys Rev B Condens Matter*, 1996, **54**, 11169–11186.
6. P. Pulay, *Molecular Physics*, 1969, **17**, 197–204.
7. S. N. Kabekkodu, A. Dosen and T. N. Blanton, *Powder Diffraction*, 2024, **39**, 47–59.
8. S. Baroni, S. de Gironcoli, A. Dal Corso and P. Giannozzi, *Reviews of Modern Physics*, 2001, **73**, 515–562.
9. A. Togo, *Journal of the Physical Society of Japan*, 2022, **92**, 012001.
10. A. Togo, L. Chaput, T. Tadano and I. Tanaka, *Journal of Physics: Condensed Matter*, 2023, **35**, 353001.
11. W. H. Press, *Numerical recipes : the art of scientific computing*, Cambridge, UK ; New York : Cambridge University Press, England, United Kingdom, 2007.
12. G. Henkelman, B. P. Uberuaga and H. Jónsson, *The Journal of Chemical Physics*, 2000, **113**, 9901–9904.
13. W. Ng, *Australian Journal of Chemistry*, 1975, **28**, 1169–1178.
14. X. Chen, X. Jin, Z. Liu, X. Ling and Y. Wang, *Energy*, 2018, **155**, 128–138.
15. N. Amghar, P. E. Sánchez-Jiménez, C. Ortiz, L. A. Pérez-Maqueda and A. Perejón, *Applied Thermal Engineering*, 2023, **235**, 121411.
16. J. Yi, R. Fu, Y. Wei and Y. Hu, *Separation and Purification Technology*, 2025, **354**, 129050.